IMA Journal of Applied Mathematics (2021) **86**, 1266–1286
https://doi.org/10.1093/imamat/hxab038
Advance Access publication on 6 September 2021

On the shape of air–liquid interfaces with surface tension that bound rigidly rotating liquids in partially filled containers

Enrique Ramé*
Madrid, 28034 Spain

Steven J. Weinstein
Department of Chemical Engineering, School of Mathematical Sciences, Rochester Institute of Technology, Rochester, NY 14623, USA

and

Nathaniel S. Barlow
School of Mathematical Sciences, Rochester Institute of Technology, Rochester, NY 14623, USA
*Corresponding author: erameche@yahoo.com

[Received on 19 February 2021; revised on 16 July 2021; accepted on 9 August 2021]

The interface shape of a fluid in rigid body rotation about its axis and partially filling the container is often the subject of a homework problem in the first graduate fluids class. In that problem, surface tension is neglected, the interface shape is parabolic and the contact angle boundary condition is not satisfied in general. When surface tension is accounted for, the shapes exhibit much richer dependencies as a function of rotation velocity. We analyze steady interface shapes in rotating right-circular cylindrical containers under rigid body rotation in zero gravity. We pay special attention to shapes near criticality, in which the interface, or part thereof, becomes straight and parallel to the axis of rotation at certain specific rotational speeds. We examine geometries where the container is axially infinite and derive properties of their solutions. We then examine in detail two special cases of menisci in a cylindrical container: a meniscus spanning the cross-section and a meniscus forming a bubble. In each case, we develop exact solutions for the respective axial lengths as infinite series in powers of appropriate rotation parameters, and we find the respective asymptotic behaviors as the shapes approach their critical configuration. Finally, we apply the method of asymptotic approximants to yield analytical expressions for the axial lengths of the menisci over the whole range of rotation speeds. In this application, the analytical solution is employed to examine errors introduced by the assumption that the interface is a right circular cylinder; this assumption is key to the spinning bubble method used to measure surface tension.

Keywords: rigidly rotating fluid interface shapes.

1. Introduction

The shapes of fluid interfaces in rigid body rotation have been well studied, with the spinning bubble tensiometer being a notable example, see Vonnegut (1942), Hu & Joseph (1994). Since about the mid-1950s, interest in such problems has grown with the need to engineer fluid containers in zero gravity for spacecraft, where guaranteeing a known location for the liquid phase is crucial for rockets to fire properly. Seebold (1965) performed a stability analysis of the menisci in circular cylindrical containers in rigid-body rotation with arbitrary axial gravity and contact angle. He derived stability limits by a variational analysis of the Hamilton principle. Later, Joseph & Preziosi (1987) analyzed the stability of

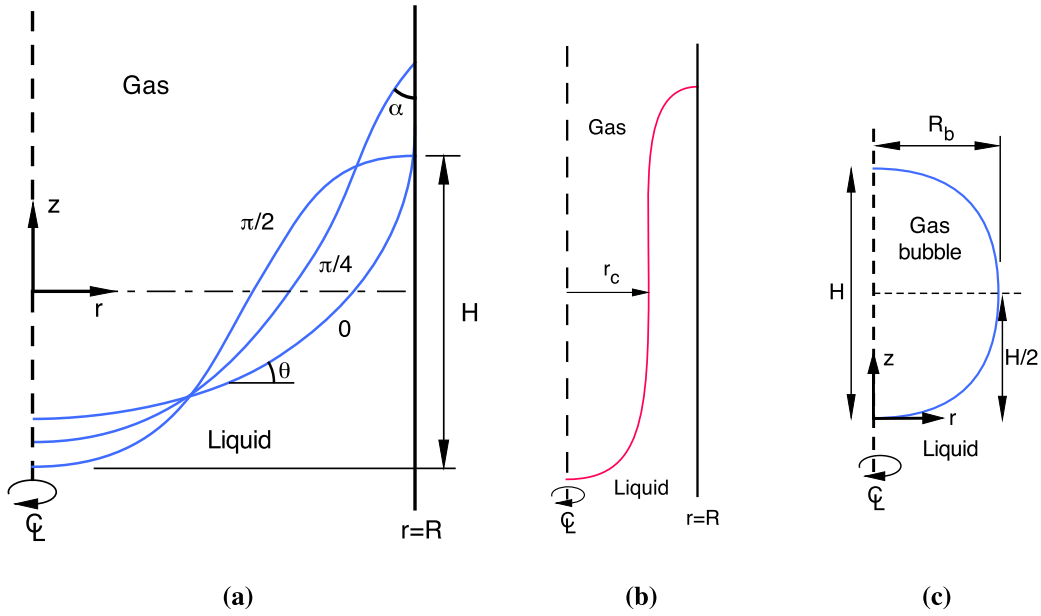

FIG. 1. Schematics of surface configurations with fluids in rigid body rotation about the axis of a cylindrical container. Liquid is below the interface. (a) Typical shapes at $\lambda < \lambda_c$, for wall contact angles, $\alpha = 0, \pi/4$ and $\pi/2$, as marked. θ is the slope angle of the interface. $z = 0$ is chosen so that the volumes of liquid above and below are equal. H is the axial meniscus length. (b) Shape with λ close to λ_c, for a 90-degree contact angle. Most of the surface is a straight circular cylinder of radius r_c. H continually increases as $\lambda \to \lambda_c$. (c) Spinning bubble. R_b is the maximum radius and H the total axial length. The half-bubble on either side of the equator is mathematically identical to the $\alpha = 0$ case in Fig. 1(a).

periodic interface shapes in rigid body rotation by minimization of an energy potential under conditions of negligible gravity, obtaining results that are wholly consistent with those of Seebold (1965).

Similar to a static meniscus in a gravitational field, the shape of the interface between two immiscible fluids in rigid body rotation with angular velocity ω, density difference $\Delta\rho \equiv \rho_1 - \rho_2$ (> 0) and surface tension σ depends on the rotational Bond number $\lambda \equiv \Delta\rho\,\omega^2 d^3/\sigma$, where d is some appropriate length that depends on the geometry being considered. The studies cited above show that a critical value λ_c exists such that, when $\lambda \to \lambda_c$ from below, the interface undergoes a critical transition, with an outcome that depends on the configuration of the fluid body and the particular container. Figure 1 illustrates some typical configurations.

More specifically, Seebold (1965) showed that the menisci having finite axial length and spanning the entire cross-section of a cylinder with contact angle α at the cylinder wall (such as shown in Fig. 1(a)) exist in zero gravity under rigid body rotation for $\lambda < 4f(\alpha)$, where $f(\alpha)$ is derived later in eq. (2.9) and satisfies $f(0) = 1$. When λ approaches $4f(\alpha)$, the meniscus reorganizes with a divergent axial length into the shape of a straight cylinder (Fig. 1(b)). Joseph & Preziosi (1987) showed that non-straight periodic interfaces that develop in rigid body motions for $\lambda < 4$ become straight cylinders when $\lambda = 4$. This result is entirely consistent with the analysis of Seebold (1965), who collected extensive experimental evidence (and also intuited without proof) that shapes become straight cylinders when $\lambda \to \lambda_c$. Ross (1968) studied the shapes of rotating drops and bubbles (as shown in Fig. 1(c)), and obtained several

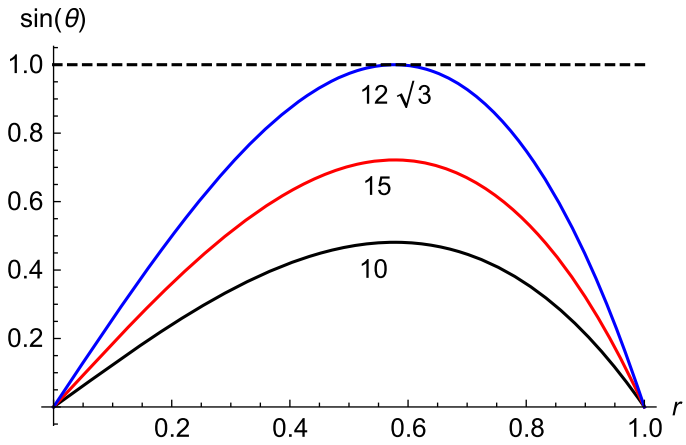

FIG. 2. Sine of the slope angle, θ (defined in Fig. 1(a)), vs. r for $\lambda = 10, 15$ and $\lambda_c = 12\sqrt{3}$. The contact angle $\alpha = \pi/2$, i.e. $\theta(1) = 0$. When $\lambda < \lambda_c$, the maximum slope corresponds to an inflection point with slope angle $0 < \theta < \pi/2$.

important results and interpretations that coincide with those of Seebold (1965) and Joseph & Preziosi (1987) in the case of bubbles and with those of Chandrasekhar (1965) in the case of drops.

In this work, we derive new features of the menisci in rigid body rotation. Specifically, our goal is to develop analytical tools to describe the axial meniscus length, denoted as H, in configurations of practical relevance as depicted in Fig. 1. We analyze two configurations: (1) a meniscus spanning the cylinder cross-section, as in Fig. 1(a and b) and (2) a meniscus forming a bubble whose axis coincides with the axis of rotation, as in Fig. 1(c). The latter geometry corresponds to that of the spinning bubble tensiometer (Vonnegut, 1942). For each geometry, we examine the respective shapes and axial meniscus lengths as a function of λ. In particular, we identify the asymptotic behaviors of the divergence in axial meniscus length as $\lambda \to \lambda_c$ and find that the divergence law depends on the meniscus configuration. We then develop exact solutions for these lengths as infinite series in powers of λ. Since these solutions converge poorly near λ_c, we apply the method of asymptotic approximants (Barlow *et al.*, 2017) to describe axial meniscus length uniformly over the whole range $0 \leq \lambda < \lambda_c$ for both configurations. We end with a discussion of implications relevant to the measurement of surface tension using a spinning bubble tensiometer.

2. Analysis

2.1 *Formulation*

Consider a liquid of density ρ in contact with a gas of negligible density in a cylindrical container of radius R, rotating with angular velocity ω about its axis in rigid body rotation (Fig. 1). The gas–liquid interface has surface tension σ, its location is $z = h(r)$ and it obeys the normal component of the dynamic boundary condition with a pressure whose gradient arises solely from centripetal acceleration.

Neglecting the dynamics of the gas and using d as a characteristic length scale, the dimensionless governing equation is given as

$$\frac{1}{r}\frac{\mathrm{d}}{\mathrm{d}r}\left(\frac{rh'}{\sqrt{1+h'^2}}\right) = -P_0 - \lambda\frac{r^2}{2}, \tag{2.1}$$

where $h'(r) = \tan\theta$ is the slope relative to the r-axis (θ is shown explicitly in Fig. 1(a)), P_0 is the pressure difference across the interface at $r = 0$ made dimensionless with σ/d and λ is the rotational Bond number, defined as

$$\lambda \equiv \frac{\rho\omega^2 d^3}{\sigma}. \tag{2.2}$$

In general, the characteristic length d depends on the configuration considered, as sketched in Fig. 1. If the interface spans the entire radius of the container, then $d = R$; for a bubble wholly surrounded by the liquid, d is the maximum radius of the bubble, R_b.

Since $h'(r) = \tan\theta$, the left-hand side of eq. (2.1) may be written as $d(r\sin\theta)/(r\,dr)$. This equation may be integrated once to obtain an expression for $\sin\theta$ as a function of r using two boundary conditions. One boundary condition accounts for the axial symmetry and is imposed to all the cases studied here:

$$\theta(0) = 0. \tag{2.3}$$

The other boundary condition is applied at the radial end of the interface. In the case of a meniscus spanning the container, the interface obeys a contact angle condition:

$$\theta(1) = \frac{\pi}{2} - \alpha, \tag{2.4}$$

where α is the contact angle, as depicted in Fig. 1(a). In the case of a bubble wholly surrounded by liquid, the second boundary condition is

$$\theta(1) = \frac{\pi}{2}. \tag{2.5}$$

Physically, this condition reflects the equatorial symmetry of the bubble; but mathematically, it can be seen to be identical to the case of a meniscus with contact angle $\alpha = 0$ expressed in eq. (2.4). The shape for arbitrary contact angle α is therefore

$$\frac{h'}{\sqrt{1+h'^2}} = \sin\theta = r\cos\alpha + \frac{\lambda}{8}r(1-r^2), \tag{2.6}$$

where, from the preceding discussion, α must be set to zero to describe a bubble. One additional integration determines $h(r)$ after a constraint specific to each configuration is applied. The axial meniscus length $H(\lambda)$ for each interface configuration is computed by integrating $h'(r)$ while taking proper account of the limits of integration. As can be seen in Fig. 1, $h(r)$ is single-valued in a meniscus spanning the container radius, and multivalued in a spinning bubble; therefore,

$$H(\lambda) = \int_0^1 h'(r)\mathrm{d}r: \quad \text{meniscus spanning container;} \tag{2.7a}$$

$$H(\lambda) = 2\int_0^1 h'(r)\mathrm{d}r: \quad \text{bubble.} \tag{2.7b}$$

2.2 *Properties of interface shapes satisfying eq. 6*

Figure 2 shows $\sin\theta$ vs. r as given by eq. (2.6) for various λ and contact angle $\alpha = \pi/2$. Qualitatively similar shapes and trends arise for shapes with arbitrary α. When $\lambda < \lambda_c$, θ attains a local maximum smaller than $\pi/2$; hence, the maximum slope angle coincides with an inflection point. However, at λ_c, the local maximum is $\theta_{\max} = \pi/2$, and the axial meniscus length diverges with infinite slope and with a straight cylindrical shape of radius equal to the location where $\theta_{\max} = \pi/2$; this is in agreement with the previous studies of e.g. Seebold (1965) and Joseph & Preziosi (1987). To find this location, we require

$$\sin\theta = 1, \quad \frac{\mathrm{d}\sin\theta}{\mathrm{d}r} = 0, \tag{2.8}$$

and obtain

$$\lambda_c = \frac{4}{r_c^3}, \quad r_c = \frac{1}{2\cos\left(\frac{1}{3}(\pi - \alpha)\right)}. \tag{2.9}$$

For $\alpha = \pi/2$, eqs. (2.9) yield $\lambda_c = 12\sqrt{3}$ and $r_c = 1/\sqrt{3}$ as in Fig. 2. Eqs. (2.9) provide exact relations in support of the numerical results of Seebold (1965) for zero gravity. In particular, if one views the vertical slope location, r_c, as the radius of a straight circular cylinder, the rotational Bond number can be written as $\overline{\lambda}_c \equiv r_c^3\lambda_c = 4$, providing a result that agrees with previous work (Joseph & Preziosi, 1987; Seebold, 1965).

Having shown that eq. (2.6) may be used both for a meniscus spanning the container with arbitrary contact angle α and for a wholly immersed bubble by setting $\alpha = 0$, in the rest of this section, we examine the case of $\alpha = \pi/2$, i.e. normal contact at the container wall. No generality is lost by focusing on this special case; on the contrary, it can be shown that, far from being special, critical shapes for arbitrary α may be obtained from the shape at any other α by suitable scaling manipulations. We now show how $\alpha = \pi/2$ generates a master shape from which all other critical shapes with $0 \leq \alpha \leq \pi$ may be constructed. The method is as follows: starting with the critical shape for $\alpha = \pi/2$, we set $\lambda = \lambda_c = 12\sqrt{3}$ and, using eq. (2.6), determine r_w such that $\theta = \pi/2 - \alpha$, i.e. r_w is the location where the critical master shape has the same θ as the wall contact slope angle of interest. Setting $\sin(\pi/2-\alpha) = \cos\alpha = (\lambda_c/8)(r_w - r_w^3)$, we find

$$r_w = \frac{2}{\sqrt{3}}\cos\left(\frac{1}{3}(\pi - \alpha)\right). \tag{2.10}$$

We then rescale r,

$$r^* = \frac{r}{r_w}. \tag{2.11}$$

Substituting for r in eq. (2.10) and manipulating to expose the binomial $(r^* - r^{*^3})$, we obtain the critical shape with $\theta = \pi/2 - \alpha$ at $r = 1$:

$$\sin\theta = r^*\cos\alpha + \frac{\lambda_c^*}{8}(r^* - r^{*^3}), \tag{2.12}$$

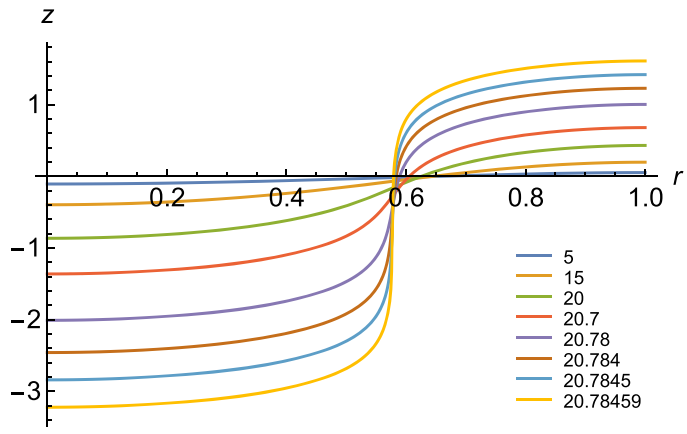

FIG. 3. Shapes with normal contact at $r = 1$ (contact angle $\alpha = \pi/2$) for values of λ noted in legend. The shape nearest $z = 0$ is for $\lambda = 5$. Consecutive values of λ apply to shapes further away from $z = 0$, showing the divergence of the meniscus axial length as $\lambda \to \lambda_c = 12\sqrt{3} \approx 20.78459....$

where λ_c^* satisfies eqs. (2.9). This is the same equation that is solved in eq. (2.6) with arbitrary α for $\lambda = \lambda_c$ and demonstrates the generality of the $\alpha = \pi/2$ result for critical shapes. Even though full meniscus shapes do not exist at $\lambda = \lambda_c$ (since the axial meniscus length H is infinite there), it is possible to use equation (2.12) to predict portions of the meniscus shape, for values of r not equal to r_c.

2.3 *Meniscus spanning the container radius*

When the meniscus spans the cylinder radius R, we identify $d = R$ in eq. (2.2). One integration of eq. (2.6) with a volume constraint fixes the absolute height of the interface. In a reference frame where the liquid volumes above and below $z = 0$ are equal, the volume condition implies:

$$\int_0^1 h\, r \mathrm{d}r = 0. \tag{2.13}$$

The computation of $h(r)$ is performed numerically by integrating $h'(r)$ given by eq. (2.6). We focus on the case of normal contact ($\alpha = \pi/2$). This case is special only because the maximum slope location is $r_c = 1/\sqrt{3}$ for all λ. Apart from this distinction, interface shapes are qualitatively similar when contact is not normal; and, as stated in Sec. 2.2, interface shapes at criticality are easily scaled across different contact angles.

2.3.1 *Meniscus asymptotics for $\lambda \to \lambda_c = 12\sqrt{3}$.* Figure 3 shows interface shapes $z = h(r)$ when $\alpha = \pi/2$. It is clear that the axial meniscus length, H, defined in eq. (2.7), diverges as $\lambda \to \lambda_c$. Identifying the leading asymptotic behavior of this divergence is of considerable theoretical and practical interest because it is relevant to control devices such as rotating reactors where two immiscible fluids of differing densities are present. Since $h'(r_c) \to \infty$ as $\lambda \to \lambda_c$, it follows that h' develops a narrowing peak around the maximum slope location, r_c, and that the area under the peak—though divergent—depends to leading order on the shape of this peak only, i.e. it is independent of the details away from

the peak. To begin, we identify the radial scale around the peak. Let

$$\epsilon \equiv \lambda_c - \lambda, \quad \eta \equiv \frac{r - r_c}{\epsilon^p}, \tag{2.14}$$

where $\epsilon \ll 1$, η is a stretched radial distance centered at the peak and p needs to be determined. Approximating h' from eq. (2.6) as $h' \sim \frac{1}{\sqrt{1-\sin^2\theta}}$ near r_c, and substituting r and λ from eq. (2.14), we find that

$$1 - \sin^2\theta \sim \epsilon \frac{\sqrt{3}}{18} + \epsilon^{2p}\, 9\, \eta^2, \quad \epsilon \to 0. \tag{2.15}$$

This suggests that, for h' to be integrable at $\eta = 0$, we must have $p = 1/2$ so that, to leading order as $\epsilon \to 0$,

$$h' \sim h'_{\text{asy}} = \frac{1}{3\sqrt{\epsilon}\sqrt{\frac{1}{54\sqrt{3}} + \eta^2}}. \tag{2.16}$$

Anticipating the presence of an $O(1)$ constant following the leading divergent behavior as $\epsilon \to 0$, we write

$$H = \int_{-\frac{1}{\sqrt{3\epsilon}}}^{(1-\frac{1}{\sqrt{3}})\frac{1}{\sqrt{\epsilon}}} \frac{\mathrm{d}\eta}{3\sqrt{\frac{1}{54\sqrt{3}} + \eta^2}} + \int_0^1 (h' - h'_{\text{asy}})\mathrm{d}r, \tag{2.17}$$

which is equivalent to the first eq. (2.7) and where in the second integral η has been written in terms of r in the expression for h'_{asy}. The first integral may be evaluated in closed form and the second one is evaluated numerically. In the limit as $\epsilon \to 0$, we obtain

$$\int_{-\frac{1}{\sqrt{3\epsilon}}}^{(1-\frac{1}{\sqrt{3}})\frac{1}{\sqrt{\epsilon}}} \frac{\mathrm{d}\eta}{3\sqrt{\frac{1}{54\sqrt{3}} + \eta^2}} \sim -\frac{1}{3}\ln\epsilon + \frac{1}{3}\ln[72(-\sqrt{3}+3)] + o(1), \tag{2.18a}$$

$$\int_0^1 (h' - h'_{\text{asy}}) \sim -0.2864 + o(1), \quad \epsilon \to 0. \tag{2.18b}$$

Combining these results,

$$H \sim H_{\text{asy}} = -\frac{1}{3}\ln\epsilon + H_0, \tag{2.19}$$

where $H_0 \approx 1.218$. Figure 4 shows the agreement between the numerical and asymptotic evaluations of the meniscus axial length.

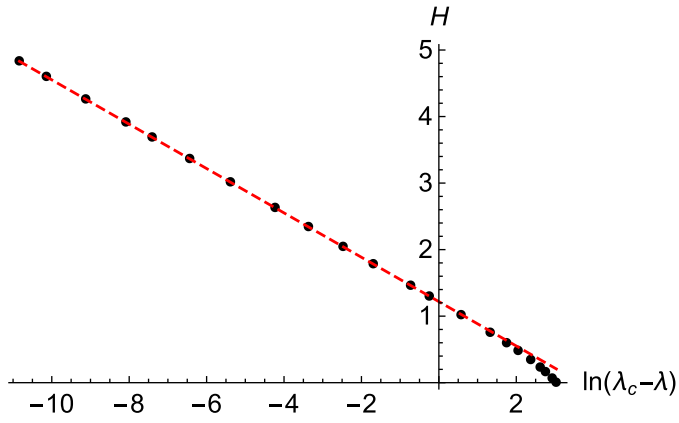

FIG. 4. Comparison of numerical and asymptotic evaluations of axial meniscus length H. $\lambda_c - \lambda = \epsilon$ and $\lambda_c = 12\sqrt{3}$. Black dots: numerical integration, eq. (2.7), with h' from eq. (2.6). Dashed line: eq. (2.19).

2.3.2 *Series solution for $H(\lambda)$.* In order to describe $H(\lambda)$ over the rest of the λ-domain, we now seek a series solution for $H(\lambda)$ in powers of λ about $\lambda = 0$. Since $h'(r,\lambda) = \tan(\theta)$, it follows that

$$h'(r,\lambda) = \frac{\sin\theta}{\sqrt{1-\sin^2\theta}}. \tag{2.20}$$

For $\alpha = \pi/2$, this expression may be expanded as a Taylor series about $\lambda = 0$ using eq. (2.6) as

$$h'(r,\lambda) = \sum_{n=0}^{\infty} a_{2n+1}(\sin\theta)^{2n+1} = \sum_{n=0}^{\infty} a_{2n+1}\left(\frac{r-r^3}{8}\right)^{2n+1}\lambda^{2n+1}, \tag{2.21}$$

where

$$a_1 = 1, \quad a_n = a_{n-2}\left(\frac{n-2}{n-1}\right), \quad n = 3,5,7,9... \tag{2.22a}$$

$$a_n = 0, \quad n = 0,2,4,... \tag{2.22b}$$

As seen in Fig. 2, $\sin\theta$ remains below 1 for $\lambda < \lambda_c$. Thus, the series in eq. (2.21) converges for $\lambda < \lambda_c$ and may be integrated term by term to obtain the meniscus length

$$H(\lambda) = \sum_{n=0}^{\infty} a_{2n+1}\, b_{2n+1}\lambda^{2n+1}, \tag{2.23}$$

where

$$b_n = \frac{1}{8^n}\int_0^1 (r - r^3)^n \mathrm{d}r, \quad n \text{ odd}, \tag{2.24a}$$

$$b_n = 0, \quad n \text{ even}. \tag{2.24b}$$

For n odd, it is easy to show that $b_1 = 1/32$ and

$$b_{n+2} = \frac{1}{64}\frac{(n+2)(n+1)\left(\frac{n+1}{2}\right)}{\left(\frac{3n+7}{2}\right)\left(\frac{3n+5}{2}\right)\left(\frac{3n+3}{2}\right)} b_n. \tag{2.25}$$

The ability to compute all the terms of the infinite series permits evaluation of the radius of convergence of the series given in eq. (2.23). The ratio test guarantees convergence iff

$$\lim_{n\to\infty} \frac{a_{2n+1}}{a_{2n-1}}\frac{b_{2n+1}}{b_{2n-1}}\lambda^2 < 1. \tag{2.26}$$

Evaluation of this criterion using eqs. (2.22a) and (2.25) shows that the series does converge for $\lambda < 12\sqrt{3} = \lambda_c$ as was stated above. Thus, eq. (2.23) is an exact solution. Unfortunately, though, the convergence is poor and nonuniform with increasing λ beyond $\lambda \approx 15$ due to the influence of a logarithmic singularity at $\lambda = \lambda_c$, see Sec. 2.3.1. In Sec. 2.5, we use asymptotic approximants to generate a rapidly converging and uniform representation of $H(\lambda)$, defined in eq. (2.7), over the entire range $0 \le \lambda < \lambda_c$.

2.4 *Spinning bubble*

If the gas volume in a finite container is small enough, or the axial dimension of the container is long enough, the bubble can become arbitrarily close to critical (i.e. it can adopt a nearly straight circular cylindrical shape with locally curved ends) before the interface touches the end plates of the container. This is the basis for the well-known spinning bubble method to determine surface tension (Hu & Joseph, 1994; Vonnegut, 1942). In this geometry (see Fig. 1(c)) and in zero gravity, bubbles exist for $\lambda < \lambda_c = 4$, and the characteristic length, d, is the maximum bubble radius, R_b. For extensive detail on the challenges of interpreting and operating the spinning drop tensiometer in a gravitational field, see Manning & Scriven (1977) and the references therein.

Using the bubble maximum radius, R_b, as the characteristic length, the slope angle of the interface relative to the r-axis is found by integrating eq. (2.6) subject to $\theta(0) = 0$, $\theta(1) = \pi/2$:

$$\sin\theta = r + \frac{\lambda}{8} r(1 - r^2). \tag{2.27}$$

Since $\sin\theta = h'/\sqrt{1 + h'^2}$, numerical integration of h' subject to $h(0) = 0$ yields the interface shape, $z = h(r)$. The bubble has infinite slope ($\theta_{\max} = \pi/2$) for all λ at $r = 1$. This contrasts the meniscus analyzed in Sec. 2.3 where $\theta_{\max} < \pi/2$ and coincides with an inflection point located in $0 < r < 1$. In this case, $\theta_{\max} \to \pi/2$ *only* as $\lambda \to \lambda_c$. To probe the character of the spinning bubble shape, we note

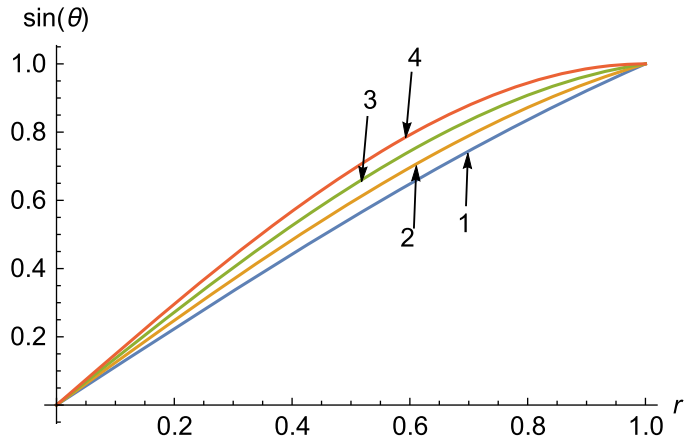

FIG. 5. Shapes of spinning bubbles at various $\lambda = 1, 2, 3, 4$. Only $\lambda = 4$ has $\mathrm{d}(\sin\theta)/\mathrm{d}r = 0$ at $r = 1$.

that, when $\lambda < 4$, a point located on the bubble's equator, denoted by $(r, \bar{z}) = (1, 0)$, corresponds to a local maximum of r. Therefore, $\mathrm{d}r/\mathrm{d}\bar{z} = 0$ and $\mathrm{d}^2r/\mathrm{d}\bar{z}^2 < 0$ there. From geometrical considerations, this implies that $1-r \sim A\bar{z}^2$, so that $\sin\theta \sim 1-2A(1-r)$ as $r \to 1$ for some constant $A > 0$. In contrast, when the shape is critical at $\lambda = \lambda_c$, the end-cap shape approaches a straight cylinder asymptotically at a distance from the bubble tip that is large compared with the radius; therefore, in the critical condition, $1 - r \sim \exp(-Bz)$ for some constant $B > 0$, where $(r, z) = (0, 0)$ is the tip location, $z \gg 1$ and the bubble is in $z > 0$. This implies that $\sin\theta \sim 1 - (B^2/2)(1 - r)^2$ as $r \to 1$ for $\lambda = \lambda_c$. We conclude, therefore, that the critical shape requires

$$\frac{\mathrm{d}(\sin\theta)}{\mathrm{d}r} = 0 \quad \text{at} \quad r = 1, \;\; \lambda = \lambda_c = 4, \tag{2.28}$$

whereas subcritical shapes satisfy

$$\frac{\mathrm{d}(\sin\theta)}{\mathrm{d}r} > 0 \quad \text{at} \quad r = 1, \quad \lambda < 4. \tag{2.29}$$

Not surprisingly, the shapes of eq. (2.27), a few of which are shown in Fig. 5, display these properties. In contrast to the meniscus spanning the cylinder radius, the distinct character of the spinning bubble configuration is that $\sin\theta = 1$ always at $r = 1$, but $\mathrm{d}(\sin\theta)/\mathrm{d}r \neq 0$ at $r = 1$ unless $\lambda = \lambda_c = 4$.

In the rest of this section, we examine the bubble axial length, $H(\lambda)$. We derive the asymptotic behavior as $\lambda \to \lambda_c$ and develop an exact solution as a series in powers of λ. Both analyses can be used to better inform the quality of the critical character of a bubble formed in an experiment.

2.4.1 *Asymptotics for* $\lambda \to \lambda_c = 4$. We derive the asymptotic behavior of the shape as $\lambda \to \lambda_c = 4$ by the same method of Sec. 2.3.1. Let $\epsilon \equiv 4 - \lambda$ and $\eta \equiv (r - 1)/\epsilon^p$, where $p > 0$ is to be determined. It may be shown from eq. 2.27 that, when ϵ is small,

$$\sin^2\theta \sim 1 - 3\epsilon^{2p}\eta^2 + \epsilon^{1+p}\frac{\eta}{2} + \ldots \tag{2.30}$$

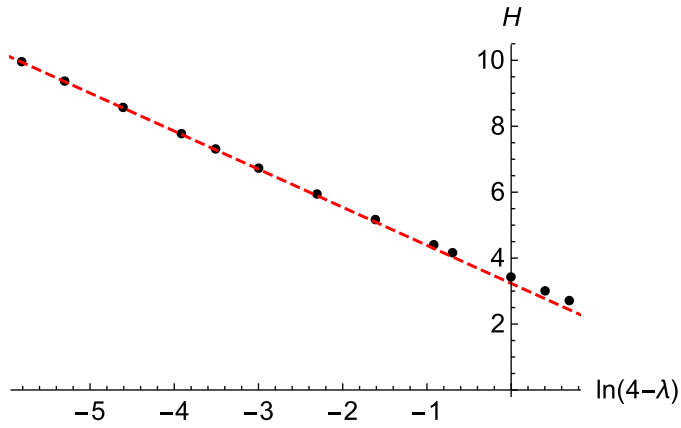

FIG. 6. Comparison of numerical and asymptotic evaluations of axial meniscus length, H, for the spinning bubble vs. λ. Black dots: numerical integration, eq. (2.7). Dashed line: asymptotics, eq. (2.32).

Approximating h' near the peak as $1/\sqrt{1-\sin\theta^2}$, the only choice that ensures integrability of h' at $\eta = 0$ is $p = 1$, yielding

$$h' \sim h'_{asy} = \frac{1}{\epsilon}\frac{1}{\sqrt{3\eta^2 - \frac{\eta}{2}}}. \tag{2.31}$$

Using the same methodology as in Sec. 2.3.1, we obtain

$$H_{asy} = \sim -\frac{2}{\sqrt{3}}\ln(4-\lambda) + 3.2332, \quad \lambda \to 4. \tag{2.32}$$

The (dimensionless) bubble volume depends on λ:

$$V(\lambda) \equiv \frac{\widetilde{V}}{R_b^3} = 2\left[\pi h(1,\lambda) - 2\pi\int_0^1 h(r,\lambda) r\,\mathrm{d}r\right] \tag{2.33}$$

and provides a relation between the dimensional volume, $\widetilde{V}$, and maximum radius R_b. The closer the bubble is to the critical configuration, the closer its shape is to a straight cylinder of dimensionless radius 1; hence, the dimensionless volume grows progressively more linearly with πH as $\lambda \to \lambda_c = 4$. The limit of eq. (2.33) as $\lambda \to 4$ is

$$V \sim \pi H - 4.18, \quad H \gg 1, \tag{2.34}$$

which is in good agreement with the asymptotic behavior of Ross' exact expression for the volume (eqn. 15 in Ross, 1968) as $\lambda \to \lambda_c = 4$; refer to Figs. 7 and 8.

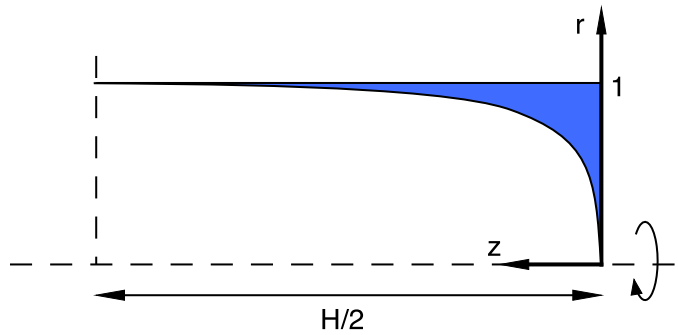

FIG. 7. Schematic of a half-bubble spinning about the z-axis. The blue area represents the liquid and is equal to the volume deficit of the actual bubble relative to a straight circular cylinder where the bubble is inscribed (see eq. (2.34)). The spinning container is larger than the bubble size and is not shown.

2.4.2 *Series solution for $H(\lambda)$.* In order to construct a Taylor series representation of the bubble axial length, defined in eq. (2.7), we note that, as in Sec. 2.3, $h' = \sin\theta/\sqrt{1-\sin^2\theta}$. However, in contrast to that analysis, here $\sin\theta \neq O(\lambda)$, which complicates evaluation of a Taylor series in powers of λ for $H(\lambda)$. Let us first generate the series

$$h'(r,\lambda) = \sum_{n=0}^{\infty} c_n(r)\lambda^n. \tag{2.35}$$

Starting from eq. (2.6), we write

$$\sin\theta = A(r) + \lambda B(r), \tag{2.36}$$

where $A = r$ and $B = \frac{r-r^3}{8}$. It follows that the denominator in the expression for $h'(= \tan\theta)$ is

$$\sqrt{1 - A^2 - 2\lambda AB - \lambda^2 B^2} = \left(\sum_{j=0}^{2} a_j \lambda^j\right)^{1/2}, \tag{2.37}$$

where $a_0 = 1 - A^2$, $a_1 = -2AB$ and $a_2 = -B^2$. Using J.C.P. Miller's formula for the series expansion of a series raised to any power (Henrici, 1956), we evaluate the series for the inverse of (2.37):

$$\left(\sum_{j=0}^{2} a_j \lambda^j\right)^{-1/2} = \sum_{j=0}^{\infty} b_j \lambda^j, \tag{2.38}$$

to find the following recursion for the coefficients,

$$\begin{aligned} c_0 &= A\, b_0 \\ c_{n>0} &= A\, b_n + B\, b_{n-1}, \end{aligned} \tag{2.39}$$

where

$$\begin{aligned} b_0 &= \frac{1}{\sqrt{1-A^2}}, \quad b_1 = \frac{AB}{\sqrt{1-A^2}}; \\ b_{n>1} &= -\frac{1}{n(1-A^2)}\left[\left(\frac{1}{2}-n\right)2A\,B\,b_{n-1} + (1-n)\,B^2 b_{n-2}\right]. \end{aligned} \tag{2.40}$$

Since c_n's are linear combinations of b_n's, convergence properties of the series in eq. (2.35) can be determined from those of $\sum_n b_n \lambda^n$. Dividing through by b_{n-1} in eq. (2.40) we form two ratios of consecutive b_n. Assuming that this ratio has a limit as $n \to \infty$, denoted $Q_\infty(r)$, the solution of a quadratic equation yields $Q_\infty(r) = (r^2 + r)/8$. Based on the ratio criterion, convergence is guaranteed with $0 \le r \le 1$ iff $\mathrm{Max}_r[Q_\infty(r)]\,\lambda < 1$, i.e. $\lambda < 4$. As in the problem of Sec. 2.3, the series in eq. (2.35) converges in the entire range of λ where shapes exist, i.e. $0 \le \lambda < 4$, and is therefore an exact solution. It can therefore be integrated term-by-term to produce another convergent exact solution for $H(\lambda)$, defined in eq. (2.7), e.g.

$$H(\lambda) = 2\sum_{n=0}^{\infty}\left(\int_0^1 c_n(r)\mathrm{d}r\right)\lambda^n = \sum_{n=0}^{\infty} C_n \lambda^n. \tag{2.41}$$

(In the appendix, we show an explicit evaluation of C_n.) Because convergence of the series in eq. (2.41) is poor as λ increases beyond $\lambda \approx 3.5$, in Sec. 2.5, we show how to implement the method of asymptotic approximants to obtain an analytical expression for $H(\lambda)$ that is uniform across the entire range $0 \le \lambda \le \lambda_c = 4$.

2.5 *Approximants*

Asymptotic approximants provide uniformly convergent approximations to the axial lengths $H(\lambda)$, as given by eq. (2.23) for a rotating meniscus and eq. (2.41) for a spinning bubble, over the entire respective intervals $0 \le \lambda \le \lambda_c$. Interested readers may consult Barlow *et al.* (2017) and the references therein for an extensive presentation of the method applied to a wide range of problems in mathematical physics.

Briefly, asymptotic approximants go beyond the well-known Padé approximants in that they incorporate asymptotic behaviors that are often singular in ways other than just poles (Bender & Orszag, 1978), thus dramatically improving the approximant's power to extend the region of convergence. Both power series for $H(\lambda)$ in the present work (eqs. (2.23) and (2.41)) have a logarithmic divergence at their respective λ_c. Because we have the power series expanded about $\lambda = 0$, as well as the logarithmic divergence behavior as λ approaches λ_c, an asymptotic approximant may be used to join these behaviors. In the two problems considered here, we propose the following approximant for $H(\lambda)$ defined in eqs.

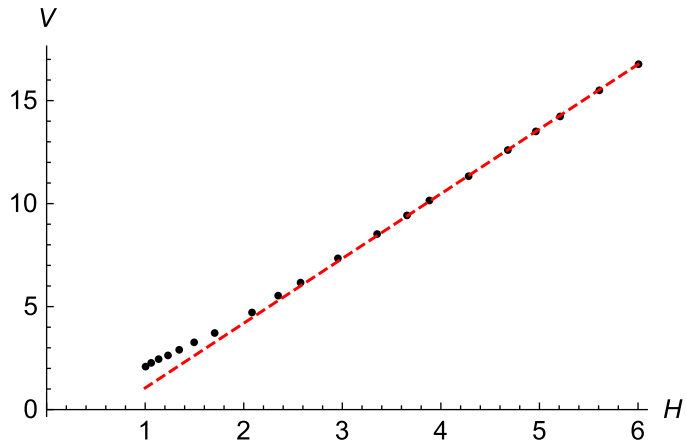

FIG. 8. Dimensionless volume, V, vs. bubble length H. Dashed line: equation (2.34).

(2.23) and (2.41):

$$H_A(\lambda, N) = \sum_{n=0}^{N} A_n(\lambda_c - \lambda)^n + A_L + B_L \ln(\lambda_c - \lambda), \tag{2.42}$$

where A_L and B_L have been computed from the respective asymptotic analyses in eqs. (2.19) and (2.32). The coefficients A_n are determined from the condition that the N-term Taylor series of $H_A(\lambda, N)$ about $\lambda = 0$ is equal to the N-term Taylor series of $H(\lambda)$ in eqs. (2.23) and (2.41). The form in eq. (2.42) imposes the asymptotic logarithmic divergence as $\lambda \to \lambda_c$.

The form of an asymptotic approximant to a given function is not uniquely determined but experience allows one to pose forms that exhibit superior convergence. In this work, we have not attempted to optimize the form of the approximant that minimizes the number of terms N required to produce a given error. Figures 9 and 10 show $H(\lambda)$ from the numerical integration of eq. (2.7) together with $H_A(\lambda, N)$, for the rotating meniscus and the spinning bubble, respectively, and for various number of terms, N, in the approximant.

We define the error of the N-term approximant, $\Delta_N(\lambda)$, as the pointwise absolute error between $H_A(\lambda, N)$ and the numerical values of $H(\lambda)$. Both approximants seem to converge to the numerical calculation as N increases, but, as shown in Figs. 11 and 12, the convergence has a small non-uniformity near λ_c. This is a well-known phenomenon due to remaining singularities that approach zero as $\lambda \to \lambda_c$ (Harkin *et al.*, 2021). The largest errors of the most accurate approximants calculated are $\Delta_{20} \approx 4 \times 10^{-4}$ for the rotating meniscus and $\Delta_{15} \approx 7.2 \times 10^{-3}$ for the spinning bubble.

3. Discussion

In configurations with arbitrary wall contact angle, α, the shape is described by eq. (2.6), rewritten here,

$$\sin\theta = r\cos\alpha + \frac{\lambda}{8}(r - r^3). \tag{3.1}$$

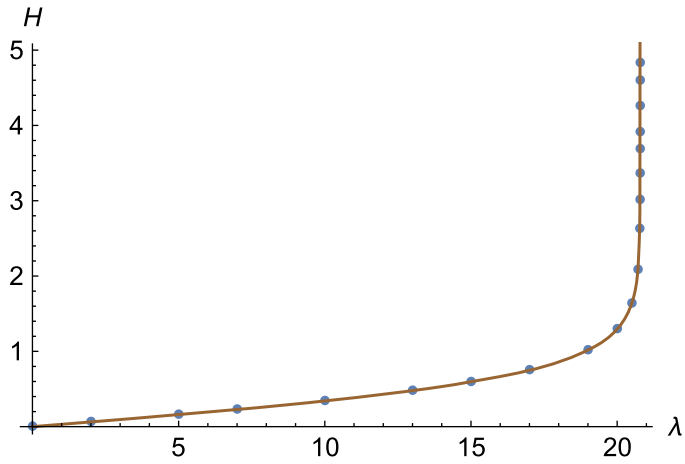

FIG. 9. The axial length of the rotating meniscus versus λ. Dots: numerical evaluation of H, eq. (2.7). Line: 20-term H_A from eq. (2.42); $A_L = 1.218, B_L = 1/3$. At $\lambda = 0$ the interface is flat, therefore $H(0) = 0$.

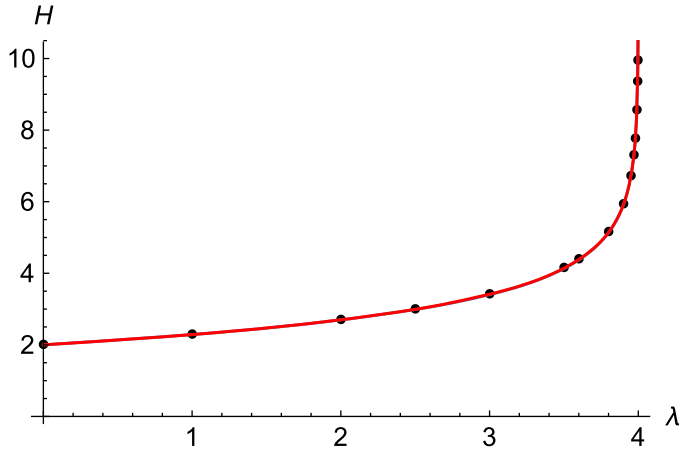

FIG. 10. The length of the spinning bubble versus λ. Dots: numerical valuation of H, eq. (2.7). Two solid lines, the 5-term and 10-term H_A, are indistinguishable; $A_L = 3.2332, B_L = 2/\sqrt{3}$. At $\lambda = 0$ and in zero gravity, the bubble is spherical, i.e. $H(0) = 2$.

Since, for the general cases of $\alpha \neq 0$, critical shapes arise from the progressive steepening of an oblique inflection point, it is instructive to find, for a given α, λ for which $\sin\theta$ has a maximum at $r = 1$; this value of λ is a lower bound for λ_c. By requiring that $\mathrm{d}(\sin\theta)/\mathrm{d}r = 0$ at $r = 1$ this value is found to be $\lambda_{\min} = 4\cos\alpha$. In order to achieve criticality in $0 < r < 1$, λ must be greater than $\lambda_{\min}$. The location of $\theta_{\max}$ for $\lambda > \lambda_{\min}$ is

$$r_0 = \left[\frac{1}{3}\left(1 + \frac{8}{\lambda}\cos\alpha\right)\right]^{1/2}. \tag{3.2}$$

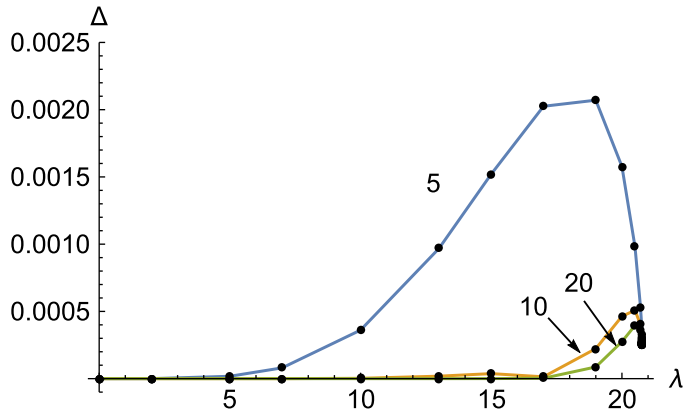

FIG. 11. Pointwise error, $|H(\lambda) - H_A(\lambda)|$, at numerically calculated points for the rotating meniscus for approximants with number of terms $N = 5, 10, 20$. Lines are indicative only and are used as a guide to the eye.

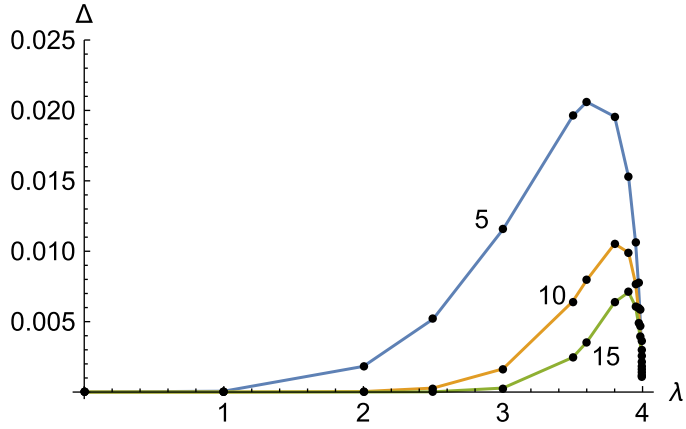

FIG. 12. Pointwise error, $|H(\lambda) - H_A(\lambda)|$, at numerically calculated points for the spinning bubble for approximants with number of terms $N = 5, 10, 15$. Lines are indicative only and are used as a guide to the eye.

Inserting this result into the expression for $\sin\theta$ above, we find the maximum value of $\sin\theta$ for a given α as function of λ:

$$\sin\theta|_{r_0} = \frac{1}{3\sqrt{3}}\,\frac{\lambda}{8}\left(1 + \frac{8}{\lambda}\cos\alpha\right)^{3/2}. \tag{3.3}$$

This expression becomes 1 when $\lambda = \lambda_c$ as given in eq. (2.9). Figure 13 illustrates this argument for $\alpha = \pi/3$. Shapes do exist for $\lambda < \lambda_{\min}$ but without an inflection point. As λ increases beyond $\lambda_{\min}$, the inflection point moves from $r = 1$ toward smaller r and the slope at the inflection becomes increasingly vertical as λ approaches λ_c. Figure 14 shows the location of the inflection (i.e. where $\sin\theta$ is maximum) versus λ.

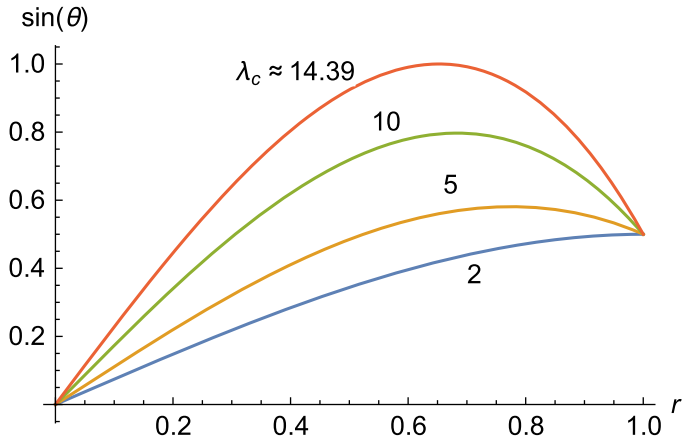

FIG. 13. Shapes for $\alpha = \pi/3$ (60-degree contact angle) for $\lambda = 2, 5, 10$ and 14.39. $\lambda_{\min} = 2$ and $\lambda_c \approx 14.39$. The location of the maximum at each λ is plotted below in Fig. 14.

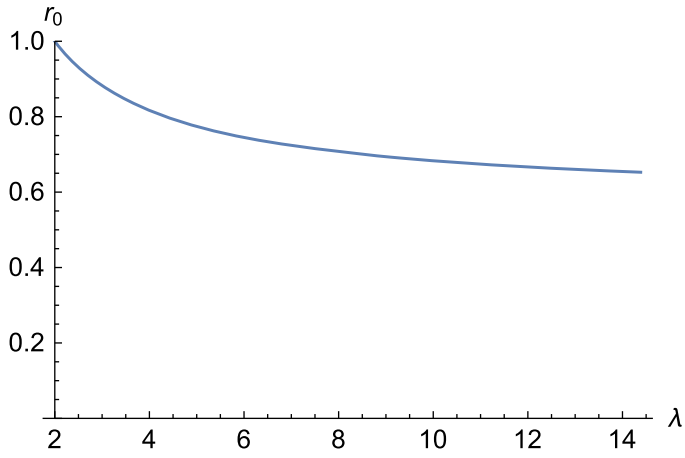

FIG. 14. r_0 vs. λ between $\lambda_{\min} = 2$ and $\lambda_c \approx 14.385$, for $\alpha = \pi/3$ (60-degree contact angle).

The axial length of the rotating meniscus has two qualitatively different configuration types. The first type is associated to contact angles larger than zero. In these cases, the radial position of the maximum slope, r_0, corresponds to an inflection point, i.e. $h'(r_0) > 0, h''(r_0) = 0$ (i.e. zero curvature) for all $\lambda < \lambda_c$; and the coefficient of the logarithmic divergence is 1/3. In general, the location of the maximum slope changes with λ for given contact angle α, as shown e.g. in Fig. 13. In the $\alpha = \pi/2$ case analyzed in Sec. 2.3.1, however, the maximum slope location is independent of λ. The second type of behavior has a single element in the zero-contact angle case. This case always has infinite slope at $r_0 = 1$, but there is a non-zero curvature at the wall for all $\lambda < \lambda_c$, given by $r''(z)$, at the contact point $r = 1$, see Fig. 1(a). The coefficient of the logarithmic divergence for the zero-contact angle case is $2/\sqrt{3}$. Perhaps more significantly, this case is mathematically identical to that of the spinning bubble.

Our results for the spinning bubble have distinctly practical implications for the measurement of surface tension by the spinning bubble tensiometer. In this method, the experimenter spins a container holding the gas–liquid pair of interest at high enough angular velocity ω that the bubble shape is nearly a straight cylinder. Then the radius, R_b, of the cylindrical bubble is measured and, assuming that $\lambda = 4$, the corresponding surface tension, denoted σ_4 to reflect the assumption just made, is obtained from

$$\lambda_c = 4 = \frac{\omega^2 R_b^3 \rho}{\sigma_4}. \tag{3.4}$$

However, for this to be valid, the bubble must be close enough to its critical configuration, which obtains when $4 - \lambda \ll 1$. Assessing this condition is not immediately obvious. In practice, an experimenter may perform several measurements at progressively higher angular velocities ω, and evaluate σ_4 each time. The measurement would be satisfactory when the value of σ_4 attains the desired accuracy—e.g. by the first n decimals remaining constant.

While the method outlined above can be used to measure the surface tension, it does not inform about the value of λ in a particular measurement. This is why the method is based on the *assumption* that $\lambda = 4$ and the experimenter must ensure that this condition is met with enough accuracy. The most direct way to find λ is to evaluate H from the ratio of bubble length to maximum radius, both of which can be measured. Using the theory, we may find λ from the function $H(\lambda)$.

Knowing the dimensional bubble volume, $\widetilde{V}$, from the difference of container volume and (incompressible) liquid volume, eq. (2.34), rewritten here as

$$\widetilde{V} \sim R_b^3 (H\pi - 4.18) \tag{3.5}$$

shows that, since H diverges when $\lambda \to \lambda_c = 4$ (eq. (2.32)), the bubble radius R_b approaches zero as $\lambda \to 4$. This is why the spinning bubble can only operate arbitrarily close to but not at $\lambda = 4$. In practical terms, when an instrument spins to produce a bubble with, say, $H = 10$ (i.e. the length is 10 times the maximum radius), the theory indicates that $\lambda \approx 4 - 2.8 \times 10^{-3}$. Since $H(\lambda)$ is a measure of how close λ is to 4, let us now consider the error in surface tension that one makes by assuming $\lambda = 4$, as a function of H. This percent error, Δ, is defined as

$$\Delta \equiv 100 \left(1 - \frac{\sigma_4}{\sigma_{\text{actual}}}\right) = 100 \left(1 - \frac{\lambda(H)}{4}\right). \tag{3.6}$$

The argument in Hu & Joseph (1994) that bubbles with $H > 4$ can be considered to be at $\lambda = 4$ is therefore inaccurate, as the present calculation predicts that $\lambda \approx 3.48$ when $H = 4$, yielding an error of 13%. Thus, a bubble with $H = 4$ is not long enough to be considered 'critical'. This is consistent with the plot of Fig. 8 where $H = 4$ is close to but not yet in the limiting long-H regime where volume increases linearly with H. However, if we make the same assumption, $\lambda = 4$, when the bubble length is $H = 10$, the error drops to 0.07%. The error of using eq. (3.4) is given by $\Delta = 411.13 \exp(-\frac{\sqrt{3}}{2} H)$, with accuracy increasing with H.

In principle, the experimenter need not assume $\lambda = 4$, however, since we now have $H(\lambda)$ (i.e. the ratio of dimensional bubble length to maximum radius, both of which can be measured), described with a uniformly convergent asymptotic approximant (see Sec. 2.5) over the entire range $0 \leq \lambda < 4$. Thus, the approximant for the bubble length allows one to extend surface tension measurement to arbitrary

values of λ with just a simple evaluation of $H_A(\lambda)$ from measurements. In the absence of gravity, the approximant allows measurements in the intermediate-λ region where the sensitivity to error in H is still moderate. But working at a lower than critical λ has the drawback that it would require precise measurements of both radius *and* length.

4. Summary and conclusion

We have examined the problem of interface shapes in fluid systems under rigid-body rotation with a focus on finding exact solutions and the asymptotics of singular behaviors near λ_c. We studied two configurations of practical importance, e.g. a meniscus spanning the rotating container radius with arbitrary contact angle at the container wall and a spinning bubble where the meniscus does not contact the container wall. Finding the asymptotic behavior of each meniscus configuration length as the critical rotation is approached as well as the series solution about $\lambda = 0$ is important because such meniscus configurations arise in applications such as a rotating reactor and a spinning bubble tensiometer. Knowing the form of the asymptotic divergence, one may construct efficient asymptotic approximants to evaluate each meniscus length at any rotation velocity uniformly and without solving a differential equation numerically.

In conclusion, this work provides analyses that advance the interpretation of interface shapes of fluids in rigid body rotation. The analyses are strictly valid in zero gravity, but their validity may be extended to normal gravity as long as the gravitational Bond number, $\rho g R^2/\sigma$, is much smaller than the rotational Bond number, λ. For two canonical configurations (meniscus spanning container radius and spinning bubble), we have found exact solutions for the axial meniscus length, H, over the whole range of λ and asymptotic behaviors near critical rotation. To remedy the poor convergence of the infinite-sum exact solutions, we constructed convergent asymptotic approximants that greatly improve the convergence efficiency of the exact solution. Our results provide proof of concept of useful analytical calculation tools for applications ranging from controlling rotating reactors to measurement of surface tension with the spinning bubble method.

Acknowledgements

Enrique Ramé is grateful to Dr R. Balasubramaniam of Case Western Reserve University for help in formulating initial ideas and calculations and for providing a critical sounding board during frequent discussions.

A. Explicit evaluation of C_n in eq. (41)

To complement the recursive evaluation of C_n of Sec. 2.4.2, in this appendix, we compute C_n explicitly. Explicit expressions (as opposed to recursive relations) may be desirable for certain types of analysis.

Because $f(r,\lambda) \equiv \sin(\theta) = r + \frac{\lambda}{8}(r - r^3) \leq 1$, we attempt expanding the denominator of $h' = f/\sqrt{1-f^2}$ as a series in powers of f. This approach is analogous to that employed in Sec. 2.3.2 but now λ is embedded in the square of the binomial f. Formally, this yields

$$h' = \frac{f}{\sqrt{1-f^2}} = \sum_{m=0}^{\infty} f^{2m+1} \frac{\Gamma(\frac{1}{2}+m)}{\sqrt{\pi}\,\Gamma(m+1)}. \tag{A.1}$$

Note that this is just the product of f times the series of even powers for the denominator. Now expand the powers of f using the binomial theorem:

$$f^{2m+1} = \sum_{i=0}^{2m+1} \frac{(2m+1)!}{i!\ (2m+1-i)!} \left(\frac{\lambda}{8}\right)^{2m+1-i} r^i (r - r^3)^{2m+1-i}. \tag{A.2}$$

A closed-form is available for the integration of the r-dependence in the above sum:

$$\int_0^1 f^{2m+1}\, \mathrm{d}r = \sum_{i=0}^{2m+1} \frac{(2m+1)!}{i!\ (2m+1-i)!} \left(\frac{\lambda}{8}\right)^{2m+1-i} \frac{\Gamma(1+m)\Gamma(2m+2-i)}{2\,\Gamma(3m+3-i)}. \tag{A.3}$$

We now use this to write the r-integral of eq. (A.1) as

$$\begin{aligned} H(\lambda) &= 2\sum_{m=0}^{\infty} \frac{\Gamma(\frac{1}{2}+m)\Gamma(2m+2)}{\sqrt{\pi}} \sum_{i=0}^{2m+1} \left(\frac{\lambda}{8}\right)^{2m+1-i} \frac{1}{2\,\Gamma(i+1)\Gamma(3m+3-i)} \\ &= \sum_{p=0}^{\infty} C_p \lambda^p. \end{aligned} \tag{A.4}$$

It remains to extract the coefficient of λ^p, C_p. Let $2m+1-i=p$. In the finite i-index sum, set $i = 2m+1-p$ for each m. It follows that the coefficient of λ^p is the result of an infinite sum:

$$C_p = \frac{1}{\sqrt{\pi}} \frac{1}{8^p} \sum_{m=m_0}^{\infty} \frac{\Gamma(\frac{1}{2}+m)\,\Gamma(2m+2)}{\Gamma(2m+2-p)\,\Gamma(2+m+p)}. \tag{A.5}$$

For a given p, the argument of $\Gamma(2m+2-p)$ in the denominator cannot be less than 1, i.e. $2m+1 \geq p$. This sets the lowest m in the sum, as $m \geq m_0 \geq (p-1)/2$. When p is odd, this condition sets the lowest m directly; when p is even, the lowest m is the smallest integer that is larger than $(p-1)/2$.

References

Barlow, N. S., Stanton, C. R., Hill, N., Weinstein, S. J. & Cio, A. G. (2017) On the summation of divergent, truncated, and underspecified power series via asymptotic approximants. *Quart. J. Mech. Appl. Math.*, **70**, 21–48.

Bender, C. M. & Orszag, S. A. (1978) *Advanced Mathematical Methods for Scientists and Engineers*. McGraw-Hill, Inc.

Chandrasekhar, S. (1965) The stability of a rotating liquid drop. *Proc. R. Soc. Lon. Ser-A*, **286**, 1–26.

Harkin, A., Giammarese, A., Barlow, N. S. & Weinstein, S. J. (2021) The Rayleigh collapse of two spherical bubbles, arXiv:2102.05222.

Henrici, P. (1956) Automatic computations with power series. *J. ACM*, **3**, 10–15.

Hu, H. H. & Joseph, D. D. (1994) Evolution of a liquid drop in a spinning drop tensiometer. *J. Colloid Interface Sci.*, **162**, 331–339.

Joseph, D. D. & Preziosi, L. (1987) Stability of rigid motions and coating films in bicomponent flows of immiscible liquids. *J. Fluid Mech.*, **185**, 323–351.

Manning, C. D. & Scriven, L. E. (1977) On interfacial tension measurement with a spinning drop in gyrostatic equilibrium. *Rev. Sci. Instrum.*, **48**, 1699–1705.

Ross, D. K. (1968) The shape and energy of a revolving liquid mass held together by surface tension. *Aust. J. Phys.*, **21**, 823–835.

Seebold, J. G. (1965) Configuration and stability of a rotating axisymmetric meniscus at low g. *Engineering Degree Thesis*. Stanford University.

Vonnegut, B. (1942) Rotating bubble method for the determination of surface and interfacial tensions. *Rev. Sci. Instrum.*, **13**, 6–9.